Available online at www.sciencedirect.com

ScienceDirect

Applied Numerical Mathematics 57 (2007) 1021–1032

APPLIED NUMERICAL MATHEMATICS

www.elsevier.com/locate/apnum

A spectral finite volume transport scheme on the cubed-sphere ☆

Vani Cheruvu [a,*], Ramachandran D. Nair [b], Henry M. Tufo [a,b]

[a] *Department of Computer Science, University of Colorado at Boulder, Boulder, CO 80309, USA*
[b] *Scientific Computing Division, National Center for Atmospheric Research, Boulder, CO 80305, USA*

Abstract

Advective processes are of central importance in many applications and their treatment is crucial in the numerical modelling of the transport of trace constituents in atmospheric models. High-order numerical methods offer the promise of accurately capturing these advective processes in atmospheric flows and have been shown to efficiently scale to large numbers of processors. In this paper, a conservative transport scheme based on the nodal high-order spectral finite volume method is developed for the cubed-sphere. A third-order explicit strong stability preserving scheme is employed for the time integration. The reconstruction procedure which we developed avoids the (expensive) calculation of the inverse of the reconstruction matrix. Flux-corrected transport algorithm is implemented to enforce monotonicity in the two-dimensional transport scheme. Two standard advection tests, a solid-body rotation and a deformational flow, were performed to evaluate the spectral finite volume method optionally combined with a flux-corrected transport scheme. Spectral accuracy in space is demonstrated with a linear wave equation.

Keywords: Spectral finite volume; Cubed-sphere; Conservative transport equation; High-order reconstruction

1. Introduction

Advection plays a fundamental role in atmospheric dynamics. In many atmospheric transport problems, a crucial step is the accurate calculation of the advective transport of atmospheric constituents over the globe. To address this goal, computational and atmospheric scientists have been attracted to devising numerical schemes which possess the following properties: (i) monotonicity, that is, the scheme should neither produce new maxima nor new minima, (ii) small numerical diffusion, (iii) mass conservation, (iv) high accuracy and (v) reasonable computational cost.

Global spectral transform methods have dominated for the past two decades in weather and climate simulation [8]. In addition to high accuracy, spherical harmonics spectral methods can provide a completely isotropic representation of a scalar function on the sphere. However, global methods based upon spherical harmonic basis functions require

---

☆ This work is supported by the DOE SciDAC program under award #DE-FG02-04ER63870 and by NSF under award #0325041. Computer time was provided by NSF ARI Grant #CDA-9601817, NSF MRI Grant #CNS-0421498, NSF MRI Grant #CNS-0420873, NSF MRI Grant #CNS-0420985, NASA AIST Grant #NAG2-1646, and the IBM Shared University Research (SUR) program. NCAR is sponsored by the National Science Foundation.

* Corresponding author. Current address: National Center for Atmospheric Research, 1850 Table Mesa Drive, Boulder, CO 80305, USA.
E-mail address: vani@ucar.edu (V. Cheruvu).

0168-9274/$30.00 © 2006 IMACS. Published by Elsevier B.V. All rights reserved.
doi:10.1016/j.apnum.2006.09.008

expensive non-local communication operations and thus have difficulty in exploiting the full potential of current high-performance parallel computers.

In recent years, research has focused on local methods that are more suitable for distributed memory parallel computers [4,3]. The need for a scheme, satisfying the above properties, led to an increase in the popularity of high-order methods, especially the spectral element (SE) method [17]. Spectral elements combine the accuracy of conventional spectral methods and the geometric flexibility of finite element methods. The SE method is not in general based on conservation laws [4] and therefore, it is not *exactly conservative* (exact in the sense of machine precision). Also, it is not trivial to incorporate monotonic limiters in SE method. For climate and atmospheric chemistry applications, the exact conservation of integral invariants such as mass and energy is crucial. The atmospheric models which are built on non-conservative forms, shown to have loss of mass over a period of time [11]. It is desirable to have a climate model based on inherently conservative numerical methods.

Cockburn et al. developed a high-order conservation algorithm, called the discontinuous Galerkin (DG) method for the nonlinear systems of conservation law (see [2] and the references therein). Recently, Nair et al. [13] proposed a conservative transport scheme on a cubed-sphere using the DG method and extended for the shallow water model [14]. The DG method requires a slope limiter if the solution has strong discontinuities. Unfortunately, there are no known efficient limiters for multidimensional DG methods of polynomial order greater than 4. As the order of the polynomial increases (i.e., as the number of nodal points increases), the ability of the conventional slope limiter to control spurious oscillation diminishes (see [7]). The lack of an efficient limiter restricts the application of high-order DG method to atmospheric flow.

Recently, Wang [19], and Wang and Liu [20,21] developed a conservative high-order spectral finite volume (SFV) method for the solution of two-dimensional systems of conservation laws. SFV method is based on classical finite volume scheme and applied to each cell (control volume) appearing in a spectral element. However, the reconstruction process is based on a high-order method. The main attraction of a finite volume approach is its ease to incorporate traditional multidimensional limiters, with which to impose monotonicity. They considered triangles for two-dimensional elements and further subdivided them into polygonal control volume cells to support high-order data reconstructions. Several types of limiters were adapted for the non-oscillatory capturing of discontinuities.

Recently, Choi et al. [1] proposed a SFV method for the numerical solution of the shallow water equations. They considered quadrilateral elements and further subdivided them into quadrilateral cells. A flux-corrected transport (FCT) scheme is incorporated to enforce monotonicity near strong discontinuities or under-resolved gradients. The reconstruction procedure in Choi et al. [1] is based on a matrix inversion. This matrix is generated from the local spectral element and may be ill-conditioned. In general application, inversion of such a matrix is not efficient.

In this paper, we developed a SFV scheme for transport equation. Our SFV scheme employs rectangular elements with high-order nodal discretization based on Gauss–Lobatto–Legendre points [9]. We used a third-order explicit strong stability preserving time integration scheme. The reconstruction procedure which we developed avoids the (expensive) calculation of the inverse of a matrix used by Choi et al. [1].

This paper is organized as follows. In Section 2, we briefly describe the transport equation in 2D and present the formulation and spatial discretization of the SFV method for rectangular elements. The FCT algorithm is reviewed in SFV context for a two-dimensional case-study. In Section 2, we also discuss our reconstruction algorithm. In Section 3, we assess the accuracy of the SFV method for a simple problem where an analytic solution is available. In this section, we show the results for the numerical implementations of the SFV method with and without an FCT limiter for two-dimensional conservation laws. In Section 4, we used this method to solve the transport equation on a cubed-sphere geometry. Finally conclusions and further investigations are summarized in Section 5.

2. The SFV method in two dimensions

Consider the two-dimensional scalar conservation law

$$\frac{\partial U}{\partial t} + \nabla \cdot \mathbf{F}(U) = 0, \quad \text{in } \mathcal{D} \times (0, T),\ \forall (x, y) \in \mathcal{D}, \tag{1}$$

where $U = U(x, y, t)$, $\nabla \equiv (\partial/\partial x, \partial/\partial y)$ is the two-dimensional gradient operator, and $\mathbf{F} = (F, G)$ is the flux function. The initial condition for the problem is $U_0(x, y) = U(x, y, t = 0)$ and the rectangular domain $\mathcal{D}$ is assumed to be periodic in both x and y directions.

2.1. SFV formulation

The SFV formulation is based on the classical finite volume method. The domain $\mathcal{D}$ is partitioned into non-overlapping spectral volumes (SVs). Let Ω be any SV in $\mathcal{D}$ which is further partitioned into non-overlapping control volumes (CVs) such that $\Omega = \bigcup \Omega_{\mathrm{CV}}$. Without loss of generality, we consider a spectral volume Ω for further discussion.

We spatially integrate equation (1) over the given control volume Ω_{CV} and apply Gauss' theorem to give the integral form of the equations

$$\int\limits_{\Omega_{\mathrm{CV}}} \frac{\partial U}{\partial t}\,\mathrm{d}A + \int\limits_{\Gamma_{\mathrm{CV}}} (\mathbf{F}\cdot\mathbf{n})\,\mathrm{d}\Gamma = 0, \tag{2}$$

where $\mathbf{n}$ is the outward unit normal to the boundary Γ_{CV} of Ω_{CV} and A is the area of the control volume bounded by Γ_{CV}. The surface integral represents the rate of change of the amount of U in Ω_{CV}, while the line integral is the total flux of U through Γ_{CV}.

Let $\bar{U}_{\mathrm{CV}}$ be the CV-averaged solution which is defined to be

$$\bar{U}_{\mathrm{CV}} = \frac{1}{A_{\mathrm{CV}}} \int\limits_{\Omega_{\mathrm{CV}}} U\,\mathrm{d}\Omega, \tag{3}$$

where A_{CV} is the area of Ω_{CV}. The finite volume form of the transport equation (1) for Ω_{CV} can now be written as:

$$\frac{\mathrm{d}\bar{U}_{\mathrm{CV}}}{\mathrm{d}t} = -\frac{1}{A_{\mathrm{CV}}} \sum_{r=1}^{N_f} \int\limits_{\Gamma_r} (\mathbf{F}\cdot\mathbf{n})\,\mathrm{d}\Gamma, \tag{4}$$

where N_f represents the number of faces in Ω_{CV} and Γ_r represents the rth face.

The preceding formulation is exact. Numerical approximation arises from evaluating the boundary integral and in time-stepping the cell averages in each CV that encompasses the domain $\mathcal{D}$.

Wang [19] discussed the stability conditions for the SFV method and compared them with that of the DG method. He showed that the CFL restriction of a second order SFV method ($\mathrm{CFL} \leqslant 1/2$) is superior to the CFL restriction of a second order DG method ($\mathrm{CFL} \leqslant 1/3$). His numerical results suggest that the third order SFV method is stable for $\mathrm{CFL} \leqslant 1/3$ versus the condition of $\mathrm{CFL} \leqslant 1/5$ in the third order DG scheme. Zhang and Shu [24] compared SFV and DG methods by first writing them in the same finite difference format over a globally uniform mesh, and then performing a Fourier type analysis for their stability, accuracy and convergence. Their conclusion is that both methods are same order accurate and stable.

2.2. Spatial discretization for rectangular elements

Let the given domain $\mathcal{D}$ be partitioned into $N_x \times N_y$ non-overlapping rectangular elements,

$$D_{pq} = \bigl\{(x, y) \mid x \in [x_{p-1/2}, x_{p+1/2}],\ y \in [y_{q-1/2}, y_{q+1/2}]\bigr\},$$

for $p = 1, 2, \ldots, N_x$, $q = 1, 2, \ldots, N_y$ such that $\mathcal{D} = \bigcup D_{pq}$. Each element D_{pq} is a SV. The extent of each SV is determined by $\Delta x_p = (x_{p+1/2} - x_{p-1/2})$ and $\Delta y_q = (y_{q+1/2} - y_{q-1/2})$ in the x and y directions, respectively. To describe the discretization, we consider a spectral volume Ω in $\mathcal{D}$. In order to take advantage of the properties of spectral methods, we have chosen our interpolation points to be Gauss–Lobatto–Legendre (GLL) points. A SV is further subdivided into $k \times k$ non-overlapping CVs by using a set of $(k+1) \times (k+1)$ GLL points. This local grid system permits the use of high-order polynomials to interpolate and reconstruct the solution in Ω. Fig. 1(a) shows a SV that is partitioned into 4×4 CVs using 5×5 GLL nodes.

An approximate solution U_Ω in any spectral volume Ω is represented as

$$U_\Omega(\xi, \eta) \approx \sum_{l=0}^{k} \sum_{m=0}^{k} U_{lm} h_l(\xi) h_m(\eta) \quad \text{for } -1 \leqslant \xi, \eta \leqslant 1, \tag{5}$$

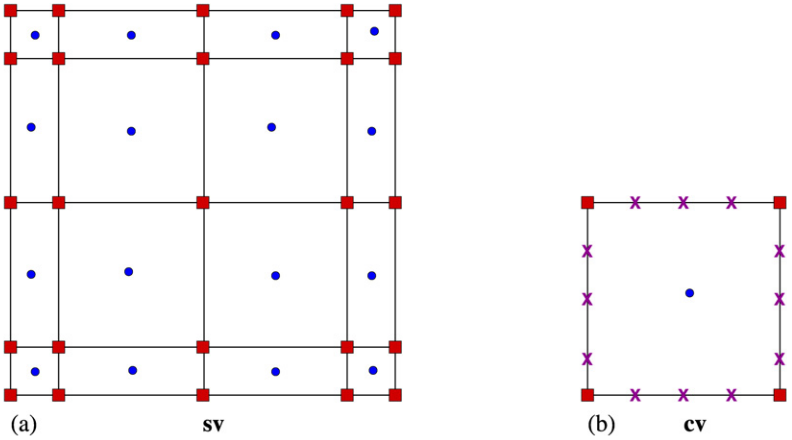

Fig. 1. Schematic of a SV with 4 × 4 CVs. (a) A SV with 5 GLL nodes (filled squares) in each direction (b) a CV with 3 Gauss points (crosses) which are used for flux evaluations.

where U_{lm} are the function values at the GLL points on Ω. The nodal basis set is constructed using a tensor-product of Lagrange–Legendre polynomials with roots at Gauss–Lobatto quadrature points [9]. The Gauss–Lobatto Lagrangian interpolation polynomial is given by

$$h_\ell(\xi) = \frac{(\xi^2 - 1)L_k'(\xi)}{k(k+1)L_k(\xi_\ell)(\xi - \xi_\ell)} \tag{6}$$

where $L_k(\xi)$ denotes the Legendre polynomial of degree k, L_k' is its derivative and ξ_ℓ refer to the $(k+1)$ Gauss–Lobatto roots which are the solution of

$$\left(1 - \xi_\ell^2\right)L_k'(\xi_\ell) = 0; \quad \ell = 0, \ldots, k. \tag{7}$$

Let Ω_{lm} denote the (l, m)th CV in Ω, defined by the interval $[\xi_{l-1}, \xi_l] \times [\eta_{m-1}, \eta_m]$. In order to evaluate the flux integrals along the CV boundaries in Eq. (4), we employ a Gauss quadrature rule. The quadrature points are interpolated from the GLL grid line using the interpolant (6). Fig. 1(b) shows a CV with cell edges being GLL nodes and 3 Gauss–Legendre nodes are used for the evaluation of the boundary integral on each side of a CV. The solid circles shown at the center of each cell in Fig. 1(a) and 1(b) indicate the cell average.

2.3. High-order reconstruction for SFV

Reconstruction is the process of finding the cell-edge values from the given cell-centered averages. This is usually performed by an interpolation operation with conservation constraints. For the SFV method, the reconstruction process should ideally be high-order and computationally efficient. In Choi [1], the reconstruction process involves matrix inversion, however such matrices need to be non-singular. Also if the matrix is not diagonally dominant then the matrix inversion may be computationally inefficient.

We introduce a reconstruction process which avoids such matrix inversion. Here we describe the reconstruction for the SFV method based on an accumulated mass approach and designed for a GLL grid system. Consider a one-dimensional grid with GLL points $\xi_\ell \in [-1, 1]$, $\ell = 0, 1, \ldots, k$. The *accumulated* mass on this grid is defined by

$$M(\xi) = \int_{-1}^{\xi} \rho(\xi)\,\mathrm{d}\xi, \tag{8}$$

where $\rho(\xi)$ is the *density* distribution function with average density for each GLL grid cell $\Delta\xi_\ell = \xi_\ell - \xi_{\ell-1}$,

$$\bar{\rho}_\ell = \frac{1}{\Delta\xi_\ell} \int_{\xi_{\ell-1}}^{\xi_\ell} \rho(\xi)\,\mathrm{d}\xi, \quad \ell = 1, 2, \ldots, k. \tag{9}$$

Then the accumulated mass (8) at each GLL grid point is given by

$$M_\ell = M(\xi_\ell) = \int_{-1}^{\xi_\ell} \rho(\xi)\,\mathrm{d}\xi = \sum_{\nu=1}^{\ell} \int_{\xi_{\nu-1}}^{\xi_\nu} \rho(\xi)\,\mathrm{d}\xi = \sum_{\nu=1}^{\ell} \overline{\rho_\nu}\Delta\xi_\nu, \quad \ell = 1, 2, \ldots, k. \tag{10}$$

From (8) it is clear that $M(\xi = -1) = M_0 \equiv 0$. Now the values M_ℓ, $\ell = 0, 1, \ldots, k$, uniquely define the accumulated mass at the GLL points. However, $M(\xi)$ can be defined in terms of the basis functions $h_\ell(\xi)$ as follows,

$$M(\xi) = \sum_{\ell=0}^{k} M_\ell h_\ell(\xi). \tag{11}$$

Eq. (8) implies that the density $\rho(\xi)$ at the cell edge is the derivative of the mass function $M(\xi)$. Thus,

$$\rho(\xi) = M'(\xi) = \sum_{\ell=0}^{k} M_\ell h'_\ell(\xi) \tag{12}$$

provides the edge values $\rho_\ell = \rho(\xi_\ell)$ by collocation differentiation, where the derivative h'_ℓ can be pre-computed [9].

The above reconstruction procedure can be extended to the 2D GLL grid (Fig. 1(a)) by a tensor-product of 1D operations. There are two stages. In the first stage, the accumulated masses $M_{l,m}$ are estimated along the ξ-direction using (10) at the CV boundaries. Then a differentiation operation (12) is applied to determine the *intermediate* edge values $\rho^*_{l,m}$. In the second stage, the intermediate values $\rho^*_{l,m}$ are used as known cell-averages and the accumulated mass $M^*_{l,m}$ in the η-direction are computed. Finally, the edge values at the GLL grid points $\rho_{l,m}$ are determined by employing (12) with $M^*_{l,m}$ as the accumulated masses. Thus, $2(k-1)$ one-dimensional operations are required for the 2D reconstruction.

2.4. Flux evaluation

Following Wang's formulation for flux evaluation [19], we need to evaluate the fluxes at each of the CV boundaries. For a given SV Ω, since the solution is continuous across the interior CV boundaries, analytic fluxes are used for the flux integral in Eq. (4). However, along the CV boundaries coinciding with the SV edges, the flux values are not uniquely defined. To address this, the analytic flux is replaced by a numerical flux by solving a Riemann problem. The numerical flux resolves the discontinuity at the SV boundaries and this is the only way by which adjacent spectral volumes communicate. A variety of flux formulae are available [18]; we employ a local Lax–Friedrichs flux formula

$$\hat{F}(U^L, U^R) = \frac{1}{2}\left[F(U^L) + F(U^R) - \bar{\alpha}(U^R - U^L)\right] \tag{13}$$

where U^L, U^R are the left and right states of solution at the interface and $\bar{\alpha}$ is the local upper bound on $|F'(U)|$. The choice of Lax–Friedrichs flux is made because of its simplicity and computational efficiency. However, this particular choice is not critical [19].

2.5. Time integration

There are a number of time integrators available to solve the ordinary differential equation in Eq. (4). We use a strong stability preserving (SSP) third-order Runge–Kutta time discretization [6]. SSP time integration schemes do not generate new local maxima or minima due to time discretization. Due to this property, these schemes are popularly used in DG literature [2]. This motivated us to consider SSP third-order Runge–Kutta time integration scheme for SFV method. For a given ordinary differential equation,

$$\frac{\mathrm{d}}{\mathrm{d}t}U = L(U) \quad \text{in } (0, T),$$

the third-order SSP scheme is given by

$$\bar{U}^{(1)} = \left[\bar{U}^n + \Delta t L\left(\bar{U}^n\right)\right],$$
$$\bar{U}^{(2)} = \frac{3}{4}\bar{U}^n + \frac{1}{4}\left[\bar{U}^{(1)} + \Delta t L\left(\bar{U}^{(1)}\right)\right],$$
$$\bar{U}^{n+1} = \frac{1}{3}\bar{U}^n + \frac{2}{3}\left[\bar{U}^{(2)} + \Delta t L\left(\bar{U}^{(2)}\right)\right], \tag{14}$$

where the superscripts n and $n+1$ denote time levels t and $t+\Delta t$, respectively.

2.6. Flux-corrected transport algorithm

High-order schemes generally produce Gibbs oscillations in regions of unresolved gradients or strong discontinuities in the solution. A FCT algorithm is incorporated to enforce monotonicity near strong discontinuities.

Zalesak [23] generalized the concept and implementation of Boris and Book's FCT algorithm to multi-dimensions. FCT was proposed as a way of approximating a conservation law with a high-order scheme in regions where the solution is smooth while using a low-order monotone scheme where the solution is poorly resolved or discontinuous. We have adopted and suitably modified this scheme to accommodate the SFV scheme for transport model. We now give the details of the SFV-FCT algorithm and present two numerical experiments involving a discontinuity.

The FCT algorithm requires the calculation of two sets of fluxes, namely low-order fluxes that yield a monotonic but diffused solution, and high-order fluxes for correcting the low-order truncation errors only where the solution is smooth. We have used the Godunov scheme [18] to calculate the low-order solution and the SFV method to calculate the high-order fluxes. The main steps in the SFV-FCT algorithm for the transport model are:

(1) Compute the cell averages $(\bar{U})^n$ for the initial condition.

(2) Compute the monotonic upwind fluxes corresponding to the Godunov scheme which are denoted by $F^l_{i+1/2,j}$ and $G^l_{i,j+1/2}$ in the x and y directions respectively.

(3) Advance the cell averages in time using the low-order fluxes to obtain the diffusive solution

$$\bar{U}^d = \bar{U}^n - \Delta t\left(F^l_{i+1/2,j} - F^l_{i-1/2,j} + G^l_{i,j+1/2} - G^l_{i,j-1/2}\right).$$

(4) Compute the high-order fluxes corresponding to the SFV scheme which are denoted by $F^h_{i+1/2,j}$ and $G^h_{i,j+1/2}$ in the x and y directions respectively. These high-order fluxes are computed using a quadrature rule as given in Section 2.2.

(5) Compute the anti-diffusive fluxes (i.e., $A_{i+1/2,j} = F^h_{i+1/2,j} - F^l_{i+1/2,j}$ and $A_{i,j+1/2} = G^h_{i,j+1/2} - G^l_{i,j+1/2}$) and limit them so that the final "anti-diffusion" step does not generate new maxima or minima. Hence,

$$A^c_{i+1/2,j} = C_{i+1/2,j}A_{i+1/2,j}, \quad 0 \leqslant C_{i+1/2,j} \leqslant 1,$$
$$A^c_{i,j+1/2} = C_{i,j+1/2}A_{i,j+1/2}, \quad 0 \leqslant C_{i,j+1/2} \leqslant 1.$$

The determination of the limiting factors $C_{i+1/2,j}$ and $C_{i,j+1/2}$ is described in detail by Zalesak [23].

(6) Perform the anti-diffusion step i.e., advance the cell averages based on the limited anti-diffusive fluxes

$$\bar{U}^{n+1} = \bar{U}^d - \Delta t\left(A^c_{i+1/2,j} - A^c_{i-1/2,j} + A^c_{i,j+1/2} - A^c_{i,j-1/2}\right).$$

The time-integrator scheme in steps (3) and (6) is the Euler forward scheme. We can see that the SSP-RK3 scheme (Eq. (14)) is a combination of three Euler forward schemes with positive weighting factors. The FCT scheme is applied in (14) in a sequential manner. Hence, the above algorithm can be extended to the SSP-RK3 scheme in Eq. (14) by repeating steps (2) to (6) for all three Euler schemes. Note that limiting in (14) is only applied to $L(\bar{U}^k)$, $k = n, 1, 2$. This avoids the redundant limiting of the already limited solution.

3. Numerical experiments

We first illustrate, by a numerical example, the spectral accuracy of the proposed SFV scheme for a smooth problem to verify correctness of the SFV scheme. We consider a test problem that is amenable to analytic solution, and the errors depend on the number of elements and on the order of interpolation.

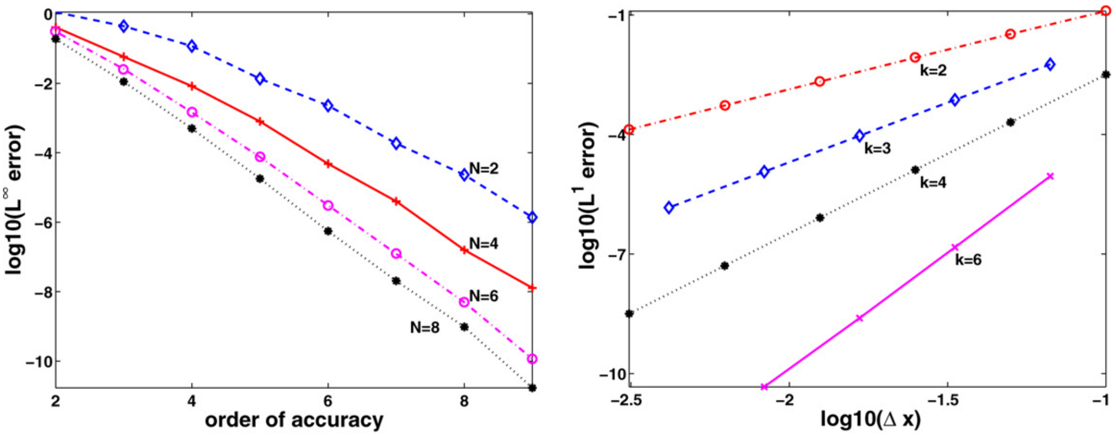

(a) (b)

Fig. 2. Demonstration of spectral accuracy with linear wave equation (a) fixed element partition: N number of elements with varying order of accuracy (b) fixed order of accuracy: k number of cells with varying number of elements.

3.1. *Accuracy study*

We consider the one-dimensional linear wave equation with constant velocity 1,

$$\frac{\partial \phi}{\partial t} + \frac{\partial \phi}{\partial x} = 0, \quad -1 \leqslant x \leqslant 1 \tag{15}$$

with initial condition $\phi(x,0) = \sin(\pi x)$, for testing the spectral convergence. Third-order SSP time-integration scheme was used for all the computations presented here and we made $\Delta t = 0.0001$ small enough so that the errors plotted in Fig. 2 are time-step independent. To demonstrate the spectral accuracy of the SFV scheme, we considered both p-refinement (see Fig. 2(a)) and h-refinement (see Fig. 2(b)). In both Fig. 2(a) and Fig. 2(b), we compared the numerical solution with the exact solution at $t = 1$. In Fig. 2(a), we fixed the number of SVs N, while the order of accuracy is increased in the SVs from $2, \ldots, 9$ (p-refinement). This figure shows the L^∞ errors versus the order of accuracy for a fixed number of elements N. In Fig. 2(b) we fixed the order of accuracy k (number of control volumes in each SV), while we increased the number of spectral volumes (h-refinement). In this figure, for a fixed order of accuracy, we considered elements of various sizes and plotted them against the L^1 errors. In both Figs. 2(a) and 2(b), it is clear that the SFV scheme attains spectral accuracy.

3.2. *Numerical tests*

We consider two standard advection tests, namely rotational and deformational flow problems in two-dimensions,

$$\frac{\partial \phi}{\partial t} + \frac{\partial (\phi u)}{\partial x} + \frac{\partial (\phi v)}{\partial y} = 0, \quad \text{in } [-\pi, \pi]^2, \tag{16}$$

where ϕ is the advecting field in the given periodic domain with the velocity (u, v) and ω is the angular velocity.

3.2.1. *Rotational flow*

We consider solid-body rotation of Gaussian hill and a non-smooth function with the velocity $(u, v) = (-\omega y, \omega x)$.

(a) Solid-body rotation of Gaussian hill.

We first consider the solid-body rotation of Gaussian hill (smooth function) to test the SFV scheme. The Gaussian-hill function at time $t = 0$, positioned at $[-\pi/2, 0]$, is defined as

$$\phi(x, y, 0) = a_0 \exp(-r^2), \quad r^2 = (x + \pi/2)^2 + y^2, \quad a_0 \in \mathcal{R}. \tag{17}$$

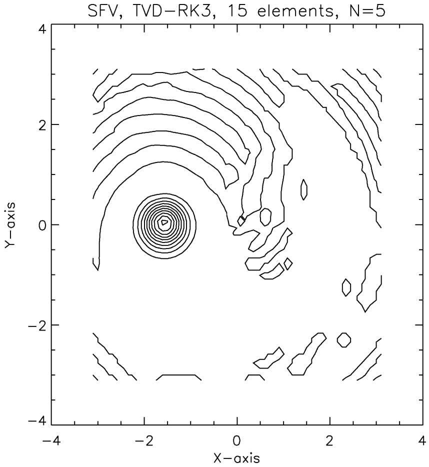

Fig. 3. Contour lines of the Gaussian Hill at the end of a single rotation using the SFV method. The simulation show the results for a 15 × 15 elemental partition of the domain and 5 GLL points (4 × 4 cells in each element).

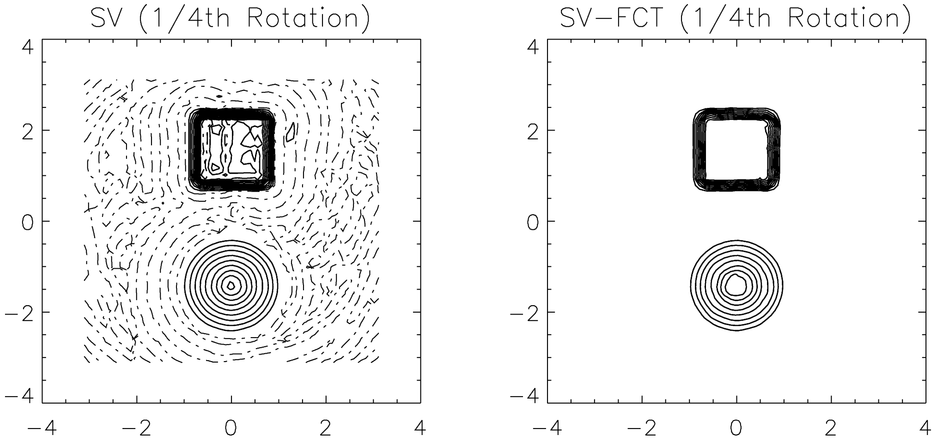

Fig. 4. Contour lines of the solid-body rotation of the function given in Eq. (18) after 1/4th of the rotation. Left panel shows the solution using the SFV scheme and the right panel shows the solution using the SFV-FCT scheme.

Fig. 3 shows the result of solid-body rotation of the Gaussian hill defined in Eq. (17) with $\Delta t = 0.0025$. Here, the solution is shown as a contour plot after one rotation with the SFV method. As observed by Iskandarani et al. [7], we found that the SFV solution is more noisy than that of the DG solution.

(b) Solid-body rotation of a non-smooth function.

We use the solid-body rotation test given in Leveque [10], to test the high-order SFV scheme. This test consists of a quasi-continuous data and provides an excellent test for the monotonicity of the advecting field. The initial data is defined as $\phi = 0$ except in a square region where $\phi = 1$ and a circular region where ϕ is cone-shaped, growing to a value 1 at the center:

$$\phi(x, y, 0) = \begin{cases} 1 & \text{if } 0.1 < x < 0.6 \text{ and } -0.25 < y < 0.25, \\ 1 - \frac{r}{0.35} & \text{if } r \equiv \sqrt{(x + 0.4)^2 + y^2} < 0.35, \\ 0 & \text{otherwise.} \end{cases} \tag{18}$$

Fig. 4 shows the result of quarter of the solid-body rotation of the function defined in Eq. (18). Here, the solution is shown as a contour plot after one quarter of the rotation for both the SFV and the SFV-FCT schemes. Without the FCT scheme, spurious oscillations generate and the solution blows up before making a complete revolution.

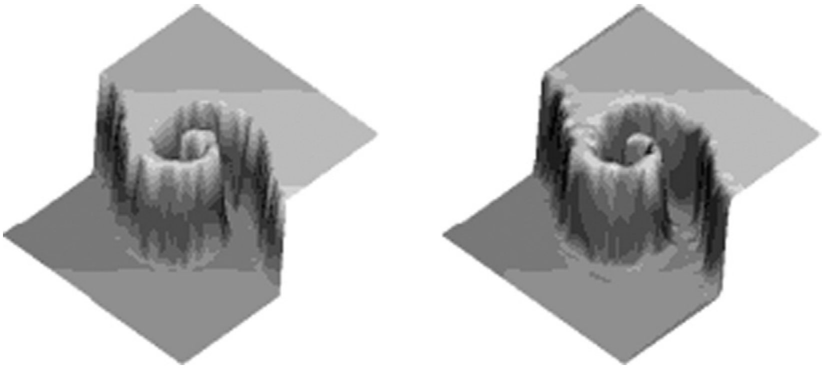

Fig. 5. The solution at time $t = 3$. Left panel shows the exact solution and the right panel shows the computed solution.

3.2.2. *Deformational flow*

We consider a well-known test in meteorology, where an idealized cyclogenesis [5] is used as a deforming field. Here, the flow field is highly deformational and more challenging than solid-body rotation. The initial discontinuous distribution is given by $\tanh(\frac{y}{\delta})$, where δ expresses the characteristic width of the front zone. For this initial distribution, the exact solution represents the rotation of a discontinuous rolling surface. The analytic solution at time t is

$$\phi(x, y, t) = -\tanh\left\{\frac{y - y_c}{\delta}\cos(\omega t) - \frac{x - x_c}{\delta}\sin(\omega t)\right\}, \tag{19}$$

where the angular velocity is $\omega = v_T/r$ and the tangential velocity is $v_T(r) = v_0 \operatorname{sech}^2(r)\tanh(r)$, with r being the radial length of the vortex and (x_c, y_c) being the center of the vortex (see [12] for detailed definition of the parameters). The value of the parameter δ is set to 0.05, which corresponds to 'non-smooth cyclogenesis'. We employed the SSP high-order accurate SFV-RK3 method with the FCT limiter to control spurious oscillations. The left panel in Fig. 5 shows the exact solution at time $t = 3$ and the right panel shows the numerical solution obtained using the Runge–Kutta SFV method with the FCT limiter at time $t = 3$.

4. Application of the SFV scheme on the cubed-sphere

4.1. *Cubed-sphere geometry*

Conventional latitude-longitude grid systems introduce singularities at the poles of the sphere. To avoid this "pole problem", atmospheric modelers are adopting new grid system such as cubed-sphere geometry [15]. Here a sphere is decomposed into six identical regions, obtained by a central projection of the faces of the inscribed cube onto the spherical surface. Each of the six local coordinate systems is free of singularities and employs the identical metric terms, thus creating a non-orthogonal curvilinear coordinate system on the sphere. Here we consider the equi-angular central projection with central angles $x^1 = x^1(\lambda, \theta)$, $x^2 = x^2(\lambda, \theta)$ such that $x^1, x^2 \in [-\pi/4, \pi/4]$ for each of the six faces, where λ and θ are the longitude and latitude coordinates, respectively.

Fig. 6 illustrates schematically the orientation of the different cube faces and their local connectivity. Lateral faces are identified by F_n, $n = 1, \ldots, 4$, whereas the top and bottom faces are F_5 and F_6 respectively. The transformation laws on the six faces of the cubed-sphere are given in [13].

Let $\mathbf{a}_1$ and $\mathbf{a}_2$ be the covariant base vectors of the transformation and $\mathbf{v}(\lambda, \theta) = (u, v)$ be the spherical velocity vector. Then the components of the covariant vectors are given by, $u_1 = \mathbf{v} \cdot \mathbf{a}_1$, $u_2 = \mathbf{v} \cdot \mathbf{a}_2$, and the corresponding contravariant vectors are related through $\mathbf{v} = u^1\mathbf{a}_1 + u^2\mathbf{a}_2$. To transform the spherical velocity (u, v) to the cubed-sphere velocity vectors, we use the following relation

$$A\begin{bmatrix} u^1 \\ u^2 \end{bmatrix} = \begin{bmatrix} u \\ v \end{bmatrix}, \qquad A^{-1}\begin{bmatrix} u \\ v \end{bmatrix} = \begin{bmatrix} u^1 \\ u^2 \end{bmatrix} \tag{20}$$

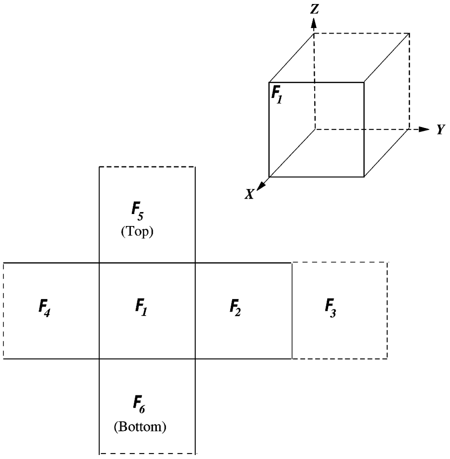

Fig. 6. Schematic illustration of the relative positions of six cube faces and their local connectivity.

where A and A^{-1} are interpreted as the "cube-to-sphere" and the "sphere-to-cube" transformation matrices. The metric tensor of the transformation is defined by

$$g_{ij} = A^{\mathrm{T}} A; \quad A = \begin{bmatrix} R\cos\theta\,\partial\lambda/\partial x^1 & R\cos\theta\,\partial\lambda/\partial x^2 \\ R\partial\theta/\partial x^1 & R\partial\theta/\partial x^2 \end{bmatrix} \tag{21}$$

and $g = \det(g_{ij})$, R is the radius of the sphere.

For the SFV formulation, each face of the cubed-sphere is partitioned into $N_e \times N_e$ rectangular non-overlapping spectral volumes. Each spectral volume is mapped onto the reference element $[-1, 1] \times [-1, 1]$, which is further divided into $k \times k$ control volumes. Hence, the total number of SVs on the cubed-sphere is $6 \times N_e^2$ and the number of CVs is $6 \times N_e^2 \times k^2$.

4.2. *Conservative transport on cubed-sphere*

The continuity equation in flux form, on the sphere, is given by

$$\frac{\partial\phi}{\partial t} + \operatorname{div}(\phi\mathbf{v}) = 0 \tag{22}$$

where ϕ is the advecting field and $\mathbf{v} = \mathbf{v}(\lambda, \theta)$ is the horizontal wind vector. Here, Eq. (22) is a particular case of the general form (1). In curvilinear coordinates, Eq. (22) can be written as [16]

$$\frac{\partial}{\partial t}(\sqrt{g}\phi) + \frac{\partial}{\partial x^1}\left(\sqrt{g}u^1\phi\right) + \frac{\partial}{\partial x^2}\left(\sqrt{g}u^2\phi\right) = 0 \tag{23}$$

where (x^1, x^2) are considered to be contravariant independent variables. Although the velocity field $\mathbf{v} = (u, v)$ is given on the surface of the sphere, the contravariant components of the velocity field are needed in (23).

4.3. *Numerical experiments*

We now perform one of the standard advection tests, known as solid-body rotation, to evaluate the SFV scheme on the cubed-sphere.

(a) Solid-body rotation of a cosine bell.

Williamson et al. [22] proposed standard test cases to evaluate and compare numerical schemes intended for global atmospheric models. They proposed the "cosine bell" problem to test the global advection schemes in spherical geom-

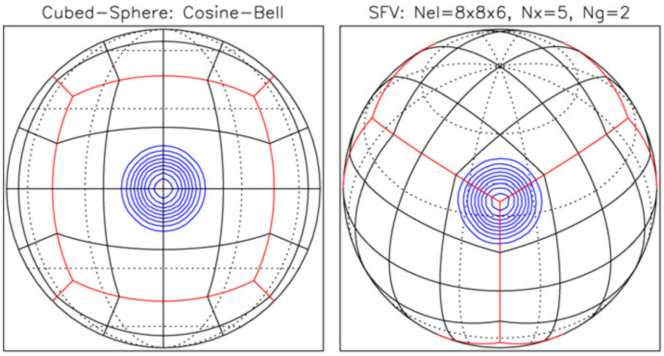

Fig. 7. Results on an orthographic projection for solid-body rotation of a cosine bell given in Eq. (24) along the northeast direction. Left panel shows the cosine bell at the initial position. Right panel shows the cosine bell when it reaches a corner point of the cubed-sphere after 1/8th of the rotation.

etry. We have used the same test for the cubed-sphere geometry where the domain has eight weak singularities (vertices of the cube) and six sub-domains. The initial scalar field is defined as follows:

$$\phi(\lambda,\theta)=\begin{cases}\frac{h_0}{2}[1+\cos(\frac{\pi r_d}{r_0})] & \text{if } r_d<r_0,\\ 0 & \text{if } r_d\geqslant r_0\end{cases}\tag{24}$$

where r_d is the great-circle distance between (λ,θ) and the bell center. The bell of radius $r_0=R/3$ is initially centered at $(3\pi/2,0)$, corresponding to the central point of F_4 on the cube. The maximum height of the cosine bell is $h_0=1000$ m and the radius of the earth is $R=6.37122\times10^6$ m. The velocity components of the advecting wind field are

$$u=u_0(\cos\alpha_0\cos\theta+\sin\alpha_0\cos\lambda\sin\theta),$$
$$v=-u_0\sin\alpha_0\sin\lambda$$

where $u_0=2\pi R/(12\text{ days})$ and α_0 is the angle between the axis of solid-body rotation and the polar axis of the spherical coordinate system (Williamson et al. [22]). When the value of α_0 is equal to zero $(\pi/2)$, the flow direction is along the equator (the north-south direction). For the cubed-sphere, the flow along the northeast direction $(\alpha_0=\pi/4)$ is more challenging, because the cosine-bell pattern passes over four vertices and two edges of the cube to complete a revolution. The left panel in Fig. 7 shows the cosine bell at the initial position. The right panel in Fig. 7 displays the numerical solution centered at the first vertex away from the initial position. The cosine bell smoothly crosses over the corner point and does not exhibit any shocks or discontinuities while passing over cube-face edges. In this experiment, the number of spectral volumes $N_e=8$, the number of control volumes $k=4$ and two Gauss quadrature points are used for the evaluation of the flux integral.

5. Summary and conclusions

Advective processes are of central importance in a wide variety of applications and their treatment is crucial in the numerical modelling of the transport of trace constituents in atmospheric models. In spite of the simplicity of the equations expressing the transport, solving the equations poses a formidable task, because we insist that the numerical solutions are high-order accurate and also satisfy a number of constraints. For instance, conservation of mass and energy is crucial for climate and atmospheric chemistry applications. Further, these applications require solutions preserving positivity and monotonicity.

In this paper, we have developed a nodal high-order spectral finite volume advective transport model on the cubed-sphere. A third-order explicit SSP scheme was employed for the time integration. We have proposed a reconstruction procedure which avoids the (expensive) calculation of the inverse of the reconstruction matrix. We have also implemented Zalesak's flux-corrected transport algorithm, to enforce monotonicity, in two-dimensional framework. Two standard advection tests, solid-body rotation and deformational flow, were performed to evaluate the SFV-FCT scheme in two dimensions. Spectral accuracy is demonstrated with a linear wave equation.

A flux form shallow water model on the cubed sphere based on the SFV method is under development. We plan to report these results in the near future.

Acknowledgements

We thank our colleagues Dr. Christiane Jablonowski and Dr. Christine Johnson for reviewing the manuscript. Authors greatly appreciate the comments of two anonymous reviewers.

References

[1] B.-J. Choi, M. Iskandarani, J. Levin, D.B. Haidvogel, A spectral finite-volume method for the shallow water equations, Monthly Weather Review 132 (2004) 1777–1791.

[2] B. Cockburn, C.-W. Shu, The Runge–Kutta discontinuous Galerkin method for convection-dominated problems, Journal of Scientific Computing 16 (2001) 173–261.

[3] J. Dennis, R.D. Nair, H.M. Tufo, M. Levy, T. Voran, Development of a scalable global discontinuous Galerkin atmospheric model, International Journal of Computational Science and Engineering (2006), in press.

[4] M.O. Deville, P.F. Fischer, E.H. Mund, High-Order Methods for Incompressible Fluid Flow, Cambridge University Press, Cambridge, 2002.

[5] C.A. Doswell III, A kinematic analysis of frontogenesis associated with a non-divergent vortex, Journal of Atmospheric Science 41 (1984) 1242–1248.

[6] S. Gottlieb, C.-W. Shu, E. Tadmor, Strong stability preserving high-order time discretization methods, SIAM Review 43 (2001) 89–112.

[7] M. Iskandarani, J.C. Levin, B.-J. Choi, D.B. Haidvogel, Comparison of advection schemes for high-order $h - p$ finite element and finite volume methods, Ocean Modelling 10 (2005) 233–252.

[8] R. Jakob-Chien, J.J. Hack, D.L. Williamson, Spectral transform solutions to the shallow water test set, Journal of Computational Physics 119 (1995) 164–187.

[9] G.E. Karniadakis, S.J. Sherwin, Spectral/hp Element Methods for CFD, Oxford University Press, Oxford, 1999.

[10] R.J. Leveque, Finite Volume Methods for Hyperbolic Problems, Cambridge University Press, Cambridge, 2002.

[11] S. Moorthi, R.W. Higgins, J.R. Bates, A global multilevel atmospheric model using a vector semi-Lagrangian finite difference scheme. Part II: Version with physics, Monthly Weather Review 123 (1995) 1523–1541.

[12] R.D. Nair, J. Côté, A. Staniforth, Monotonic cascade interpolation for semi-Lagrangian advection, Quarterly Journal of Royal Meteorological Society 125 (1999) 197–212.

[13] R.D. Nair, S.J. Thomas, R.D. Loft, A discontinuous Galerkin transport scheme on the cubed-sphere, Monthly Weather Review 133 (2005) 814–828.

[14] R.D. Nair, S.J. Thomas, R.D. Loft, A discontinuous Galerkin global shallow water model, Monthly Weather Review 133 (2005) 876–888.

[15] C. Ronchi, R. Iacono, P.S. Paolucci, The "Cubed sphere": A new method for the solution of partial differential equations in spherical geometry, Journal of Computational Physics 124 (1996) 93–114.

[16] R. Sadourny, Conservative finite-difference approximations of the primitive equations on quasi-uniform spherical grids, Monthly Weather Review 100 (1972) 136–144.

[17] M. Taylor, J. Tribbia, M. Iskandarani, The spectral element method for the shallow water equations on the sphere, Journal of Computational Physics 130 (1997) 92–108.

[18] E.F. Toro, Riemann Solvers and Numerical Methods for Fluid Dynamics, Springer, Berlin, 1999.

[19] Z.J. Wang, Spectral (finite) volume method for conservation laws on unstructured grids. Basic formulation, Journal of Computational Physics 178 (2002) 210–251.

[20] Z.J. Wang, Y. Liu, Spectral (finite) volume method for conservation laws on unstructured grids: Extension to two-dimensional scalar equation, Journal of Computational Physics 179 (2002) 665–697.

[21] Z.J. Wang, Y. Liu, Spectral (finite) volume method for conservation laws on unstructured grids: One-dimensional systems and partition optimization, Journal of Scientific Computing 20 (2003) 137–157.

[22] D.L. Williamson, J.B. Drake, J.J. Hack, R. Jakob, P.N. Swarztrauber, A standard test set for numerical approximations to the shallow water equations in spherical geometry, Journal of Computational Physics 102 (1992) 211–224.

[23] S.T. Zalesak, Fully multidimensional flux-corrected transport algorithms for fluids, Journal of Computational Physics 31 (1979) 335–362.

[24] M. Zhang, C.-W. Shu, An analysis of and a comparison between the discontinuous Galerkin and the spectral finite volume methods, Computers and Fluids 34 (2005) 581–592.